Author(s): Richardson, Paul; Marin, Riccardo; Zhang, Yixin; Gabidullin, Bulat; Ovens, Jeffrey; Moilanen, Jani O.; Murugesu, Muralee

Title: Asymmetric Ring Opening in Tetrazine-based Ligand Affording a Tetranuclear Opto-Magnetic Ytterbium Complex

Year: 2021

Version: Accepted version (Final draft)

Please cite the original version:

Richardson, P., Marin, R., Zhang, Y., Gabidullin, B., Ovens, J., Moilanen, J. O., & Murugesu, M. (2021). Asymmetric Ring Opening in Tetrazine-based Ligand Affording a Tetranuclear Opto-Magnetic Ytterbium Complex. Chemistry : A European Journal, 27(7), 2361-2370. https://doi.org/10.1002/chem.202003556

Chemistry
A European
Journal

Chemistry Europe
European Chemical Societies Publishing

Accepted Article

Title: Asymmetric Ring Opening in Tetrazine-based Ligand Affording a Tetranuclear Opto-Magnetic Ytterbium Complex

Authors: Muralee Murugesu, Paul Richardson, Riccardo Marin, Yixin Zhang, Bulat Gabidullin, Jeffrey Ovens, and Jani O. Moilanen

To be cited as: *Chem. Eur. J.* 10.1002/chem.202003556

Link to VoR: https://doi.org/10.1002/chem.202003556

WILEY-VCH

10.1002/chem.202003556

WILEY-VCH

FULL PAPER

Asymmetric Ring Opening in Tetrazine-based Ligand Affording a Tetranuclear Opto-Magnetic Ytterbium Complex

Paul Richardson,[a] Riccardo Marin,[a] Yixin Zhang,[a] Bulat Gabidullin,[a] Jeffrey Ovens,[a] Jani O. Moilanen,[b] and Muralee Murugesu*[a]

[a] P. Richardson, Dr. R. Marin, Y. Zhang, Dr. B. Gabidullin, Dr. J. Ovens, Prof. Muralee Murugesu
Department of Chemistry and Biomolecular Sciences
University of Ottawa
10 Marie-Curie Pvt., Ottawa, Ontario, K1N 6N5 (Canada)
E-mail: m.murugesu@uottawa.ca
[b] Dr. J. O. Moilanen
Department of Chemistry, Nanoscience Centre
University of Jyväskylä
P.O. Box 35, FI-40014 (Finland)

Supporting information for this article is given via a link at the end of the document.

Abstract: We report the formation of a tetranuclear lanthanide cluster, $[Yb_4(bpzch)_2(fod)_{10}]$ (**1**), which occurs from a serendipitous ring opening of the functionalized tetrazine bridging ligand, bpztz (3,6-dipyrazin-2-yl-1,2,4,5-tetrazine) upon reacting with $Yb(fod)_3$ (fod^- = 6,6,7,7,8,8,8-heptafluoro-2,2-dimethyl-3,5-octandionate). Compound **1** was structurally elucidated *via* single-crystal X-ray crystallography and subsequently magnetically and spectroscopically characterized to analyse its magnetisation dynamics and its luminescence behaviour. Computational studies validate the observed M_J energy levels attained by spectroscopy and provides a clearer picture of the slow relaxation of the magnetisation dynamics and relaxation pathways. These studies demonstrate that **1** acts as a single-molecule magnet (SMM) under an applied magnetic field in which the relaxation occurs *via* a combination of Raman, direct, and quantum tunnelling processes, a behaviour further rationalized analysing the luminescent properties. This marks the first lanthanide-containing molecule that forms by means of an asymmetric tetrazine decomposition.

In the era of data digitalisation and integrated electronics, miniaturisation is an urgent matter. The success of this effort towards decreasing the size of current devices is contingent upon the design of suitable nanomaterials and molecules. To that end, lanthanide single-molecule magnets (Ln-SMMs) are poised to be part of the toolkit for the preparation of next generation high-density information storage devices.[1,2] The recent discovery of a dysprosium metallocene cation $[(Cp^{iPr5})Dy(Cp^*)]^+$ (Cp^{iPr5} = penta-iso-propylcyclopentadienyl, Cp* = pentamethylcyclopentadienyl) acting as a magnet above liquid N_2 temperature is a step towards that direction.[2] This unrivalled performance of Ln-SMMs as nanomagnets is often complemented by photoluminescent properties,[3] which offer a means to overcome in operando addressability issues in terms of system temperature and applied magnetic field. Moreover, Ln-SMMs are ideal platforms for fundamental investigations around opto-magnetic cross-effects,[3,4] which can open the door to the development of novel multifunctional molecular species. This "added value" of opto-magnetic Ln-SMMs represents the drive for this study, where we report a luminescent SMM based on Yb^{3+} and tetrazine ligands.

Among the lanthanide ions explored for the preparation of luminescent Ln-SMMs,[5-8] the late Kramers ion Yb^{3+} has shown great promise. Recently, two examples of luminescent Yb-SMMs with built-in thermometric capability were published.[9,10] Furthermore, a molecular ferroelectric Yb^{3+} complex possessing room temperature magnetoelectric coupling, a rarity for molecular compounds, was reported recently by Long and co-workers.[11] These studies highlight the potential of Yb^{3+} in the development of next-generation multifunctional coordination compounds.

In those molecular species, the organic moieties (ligands) are carefully chosen to predictably modulate the physical properties of the final compound.[12-14] However, serendipitous transformation of the ligand might occur upon interaction with the metal centre. This is well highlighted in the family of 1,2,4,5-tetrazine-based ligands.[15-22] These molecules are of interest in coordination chemistry due to their facile functionalisation and their redox activity, which can enhance magnetic communication between metal ions.[23-26] For these reasons, the quest for tetrazine-based compounds is an extremely active field of research in coordination chemistry.

Depending on the functional groups present on the 1,2,4,5-tetrazine scaffold, discrete molecular species or polymeric structures may be targeted. Towards that end, the ligand 3,6-dipyrazin-2-yl-1,2,4,5-tetrazine (bpztz) is an attractive candidate. This ligand has been studied primarily in silver-containing polymers.[27,28] To our knowledge, it has only been isolated in a molecular $[Re_2]$ dimer once,[29] and Ln-based complexes are yet to be reported.

Intrigued by the scarcity of studies employing this ligand, we attempted the synthesis of a bpztz-based Yb^{3+} complex. Much to our surprise, instead of isolating a compound containing bpztz, we were met with the formation of an Yb^{3+} tetranuclear complex

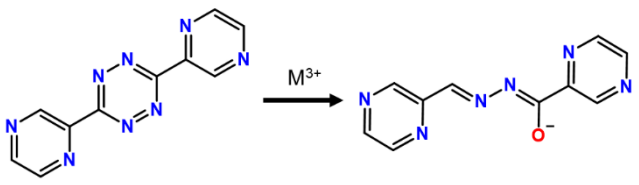

Scheme 1. Simplified reaction scheme highlighting the metal-assisted hydrolysis which lead to the ligand transformation from 3,6-dipyrazin-2-yl-1,2,4,5-tetrazine (bpztz, left) to *N'*-[(*E*)-pyrazin-2-yl)methylidene]pyrazine-2-carbohydrazonate (bpzch, right).

$[Yb_4(bpzch)_2(fod)_{10}]$ (**1**, bpzch = *N*'-[(*E*)-pyrazin-2-yl)methylidene]pyrazine-2-carbohydrazonate, fod^- = 6,6,7,7,8,8,8-heptafluoro-2,2-dimethyl-3,5-octandionate), where the bpztz was transformed into a new ligand, bpzch (Scheme 1). Compound **1** marks the first lanthanide-containing molecule formed through asymmetric tetrazine decomposition. Through a combined structural, magnetic, and spectroscopic characterisation, also supported by theoretical modelling, the opto-magnetic properties of the compound were elucidated. This in-depth analysis of **1** not only allowed the determination of the energy levels of the metal centres through photoluminescence studies and theoretical calculations, but also rationalized the magnetic relaxation dynamics observed for **1**.

Results and Discussion

Structural analysis

The reaction of two equivalents of anhydrous $Yb(fod)_3$ with and equivalent of bpztz in the presence of $CoCp_2$ in a N_2 atmosphere lead to the isolation of dark orange prismatic crystals suitable for single crystal X-ray diffraction studies after one week. The molecular structure of the tetranuclear compound, $[Yb_4(bpzch)_2(fod)_{10}]$ (**1**), is presented in Figure 1 (crystallographic tables, selected bond distances, and selected bond angles can be found in the Supporting Information). The compound **1** crystallizes in the *P*-1 space group with one molecule in the unit cell and consists of four Yb^{3+} metal ions bridged together by two bpzch ligands, which are transformed from the original bpztz ligand. The central core of **1** is a parallelogram with angles of ∠Yb1-Yb2-Yb1' = 115° and ∠Yb2-Yb1-Yb2' = 65° between the metal centres, respectively. The complex possesses a centre of symmetry in the centre of the core parallelogram through which two Yb^{3+} metal centres, one bpzch bridging ligand, and five fod^- co-ligands are generated. Both crystallographically distinct Yb metal centres are eight-coordinate. The Yb1 is chelated by one bpzch ligand through one of the pyrazine rings and the nitrogen atom (N4) of what was previously a tetrazine ring. Its coordination sphere is completed by three fod^- co-ligands. The Yb2 metal centre is coordinated by to three donor atoms (N1, N3, O11) from bpztz ligand, forming two five-membered chelate rings in a terpyridine-like fashion. The metal centre is also bridged through the pyrazinyl functional group of the second bpzch ligand, connecting the two halves of the molecule. Its coordination sphere is completed by two fod^- co-ligands. Both metal ions adopt distorted slightly distorted square antiprism geometry (CShM = 0.52 and 1.19 for Yb1 and Yb2 respectively; Table S4 and Figure S1 in the Supporting Information) as commonly observed in lanthanide coordination compounds.[30]

The four Yb^{3+} metal centres lie in a plane which forms in the centre of the molecule. The bridging ligands bpzch are slightly angled through the plane, while this central plane is covered on top and bottom by the fod^- co-ligands. The most striking structural feature of **1** is the hydrolysed bpzch ligand. The initial ligand bpztz has undergone an asymmetric ring opening, with the loss of an N_2 molecule and the gain of one O atom, bonded to C56. Due to the anaerobic conditions utilized to synthesize **1**, the O11 atom is likely due to the presence of a trace amount of water in the reaction mixture.[15,17,22] Along with the loss of the N_2 molecule and the opening of the ring, there is a shift in aromaticity. The central atoms N3 and N4 are now connected through a single bond to each other (d_{N3-N4} = 1.38 Å) and are further bound to a carbon atom. Each carbon connects a pyrazine ring to the ring-opened central moiety. The C55 carbon atom is further bound to a hydrogen atom and N3 (d_{C55-N3} = 1.28 Å), while C56 is bonded to N4 and O11 (d_{C56-N4} = 1.33 Å, $d_{C56-O11}$ = 1.26 Å). The deviations of d_{C56-N4} and $d_{C56-O11}$ away from the ideal carbon-nitrogen or carbon-oxygen double bond distance is indicative of aromaticity between the three atoms of this system. This is further confirmed by the bond angle between O11, C56, and N4 ($\angle_{O11-C56-N4}$ = 126°) which is consistent with an sp^2 – hybridized carbon atom. However, due to the similarity in electron density between nitrogen and oxygen, it is possible for the two atoms to be misconstrued accidentally through crystal structure refinement. However, if O11 was changed to nitrogen during the refinement process, the observed thermal ellipsoids no longer gave reasonable parameters, indicating the element is most likely oxygen. The decomposition of the central tetrazine ring of bpztz is likely metal-assisted, as similar behaviour has been observed in other 1,2,4,5-tetrazine-based ligand systems.[15-22] However, to the best of our knowledge, such an asymmetric ring opening not been previously observed in the presence of lanthanides. Due to the Yb^{3+} metal centres, **1** possesses the potential to have both interesting magnetic and/or photoluminescence properties, making it the first such asymmetric tetrazine ring-opened compound to possess opto-magnetic behaviour. Towards that end, in order to determine and compare the energy levels of the complex and have a more complete understanding of any luminescent or magnetic behaviour, we performed static and dynamic magnetic measurements, photoluminescence studies, and theoretical calculations for **1**.

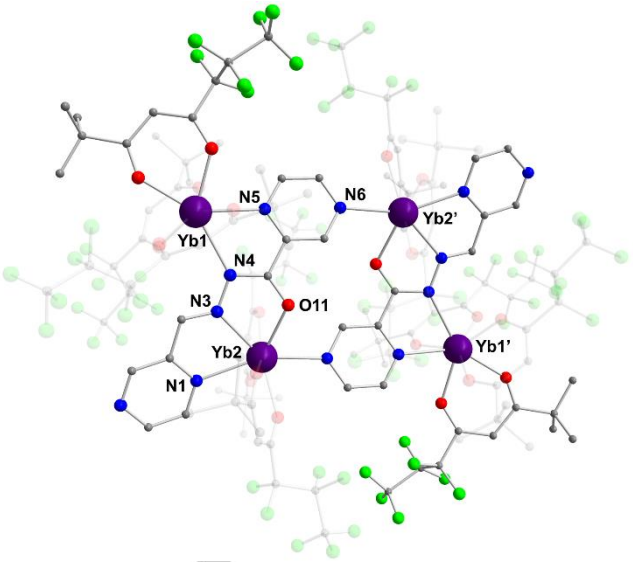

Figure 1. Partially labelled molecular representation of compound **1**. fod^- co-ligands which penetrate and protrude from the plane of the figure are presented as transparent for ease of view and to highlight the bridging motif of the transformed bpztz ligand, bpzch. H atoms have been omitted for clarity. Colour scheme: Yb, purple; F, green; O, red; N, blue; C, grey.

dc magnetic susceptibility

10.1002/chem.202003556

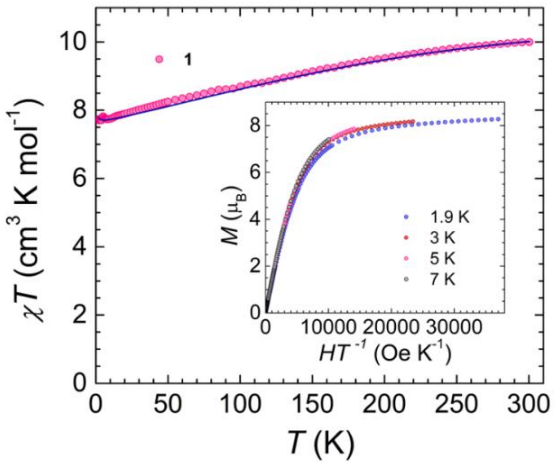

Figure 2. Temperature dependence of the χT product of **1** at 1000 Oe. The line is the best fit curve of the susceptibility. (inset) *M* vs. HT^{-1} behaviour of **1**.

Static magnetic studies were performed for **1** under an applied direct current (dc) field of 1000 Oe in a temperature range from 1.8 – 300 K. The molar magnetic susceptibility *versus* temperature (χT *vs*. *T*) data can be seen in Figure 2. The room temperature χT value of 9.88 cm^3 K mol^{-1} is close to the expected value of 10.28 cm^3 K mol^{-1} for four non-interacting Yb^{3+} metal ions. (χT_{RT} = 2.57 cm^3 K mol^{-1}, $^2F_{7/2}$, g_J = 8/7). As the temperature decreases, the χT product also decreases down to 5.85 cm^3 K mol^{-1}. This behaviour is typically attributed to a combination of weak antiferromagnetic interactions, the presence of magnetic anisotropy, and the depopulation of excited M_J levels. However, the theoretically determined intramolecular exchange and dipolar interactions obtained from the Ising model between Yb^{3+} ions are less than ±0.3 cm^{-1} indicating only a weak magnetic interaction between the metal centres with the dominant contribution arising from the antiferromagnetic coupling J_1 (Table S5 and Figure S2). Furthermore, magnetisation *versus* field measurements (*M vs. H*, Figure S3; *M vs*. HT^{-1}, Figure 2, inset) were performed to further assess the dc magnetic behaviour. The isothermal curves seen in the plot of *M vs.* HT^{-1} are not completely superimposed, indicating that presence of magnetic anisotropy originating from the heavy lanthanide ions. In comparison with the experimental data, the *ab initio* calculations predict the g_z value of ground Kramers doublets (KDs) of Yb1 (g_z = 7.365) and Yb2 (g_z = 7.826) ions to be close the expected value of 8.00 for the highly axial system with M_J = ± 7/2 state. However, closer inspection of the *g*-tensors of Yb1 and Yb2 reveals that they have also non-negligible transverse components in their *g*-tensors of ground KDs that suppress the anisotropy of Yb1 and Yb2 ions (see theoretical calculations). Such low axiality is not surprising due to the distorted nature of the SAP geometry of the metal centres. The above data shows the decrease in the χT product most likely occurs through a combination of magnetic anisotropy and the depopulation of M_J states, which is further enhanced by weak magnetic interactions. .

ac magnetic susceptibility

The magnetic relaxation behaviour of **1** was probed using alternating current (ac) magnetic susceptibility studies. These measurements were performed either at a constant temperature (2 K) with varying applied dc magnetic field, or at a constant applied dc field with varying temperature. When the measurement was performed under zero dc field, no out-of-phase signal was observed in the susceptibility. This indicates that under these conditions, quantum tunnelling of magnetisation (QTM) is the dominant pathway for reversal of the spin. Field-dependent SMM behaviour is quite common in Yb^{3+}-based molecular systems, regardless of the ligand system coordinated to the metal ions.[31-35]. Indeed, upon application of a dc magnetic field, a single high-frequency out-of-phase signal was observed up to 0.2 T, at which point a second low-frequency signal revealed itself, up to 0.46 T (Figure 3a, Figure S4 for χ' in-phase susceptibility). The field-dependence of the high-frequency peak indicates the presence of a single relaxation process at low fields, with a second magnetic relaxation mechanism revealing itself at higher fields. The data was fit to either a generalized Debye or a double Debye model where appropriate. Through these measurements it was determined that an applied dc field of 0.15 T was sufficient to minimize QTM and to probe the frequency-dependent behaviour of the slow relaxation of the magnetisation. When performed under an applied dc field of 0.15 T, frequency-dependent out-of-phase signals were observed from 5 K down to 1.8 K in a frequency range of 0.1 to 1500 Hz (Figure 3c). These plots were fit to a generalized Debye model. Values of α (distribution of curve) and τ (relaxation times) were extracted from all fits of the real (χ') and imaginary (χ'') components of the ac magnetic susceptibility (Figures S5 through S7 and Tables S6 through S8). In order to understand the specific mechanisms of magnetic relaxation in compound **1**, plots of τ *vs*. *H* and *T* respectively were made. The error bars associated with each value of τ was calculated utilizing the extracted value of α for each point and the methods outlined by Reta and Chilton.[36] It is important to note that due to the large error bars associated with extracted values of α and τ, the analysis of the magnetic relaxation pathways is primarily of qualitative use. Magnetic relaxation behaviour is typically characterized by some or all the four terms found in the following equations:

$$\tau^{-1} = \tau_{Orbach}^{-1} + \tau_{Raman}^{-1} + \tau_{Direct}^{-1} + \tau_{QTM}^{-1} \quad (1)$$

$$\tau^{-1} = \tau_o \exp\frac{-U_{\text{eff}}}{k_B T} + C\left(\frac{1+C_1H^2}{1+C_2H^2}\right)T^n + AH^mT + \frac{B_1}{1+B_2H^2} \quad (2)$$

Where equation 2 shows the specific parameters that make up the respective terms.[37] The Orbach term (first expression in equation 2) only shows temperature-dependence and provides information regarding the magnitude of the effective energy barrier between M_J states, U_{eff}. The quantum tunnelling term (final expression in equation 2) shows only field-dependence. However, both the Raman and direct magnetic relaxation processes (second and third terms in equation 2, respectively) have field- and temperature-dependence. Depending on the nature of the sample, at least one if not multiple relaxation processes may be observed in each compound. Therefore, equation 2 can be used to fit both field- and frequency-dependent extracted magnetic relaxation times. In order to fit the two magnetic relaxation plots for compound **1**, equation 2 was initially tested utilizing each of the terms on their own, then subsequently through combination of multiple terms to improve the fit. The use of an Orbach term at any point in the fits did not provide reasonable values for U_{eff} and did not improve other fits when employed. This is consistent with the low temperatures where magnetic relaxation is observed, as the Orbach process is thermally activated. However, when initial fits of both Raman and QTM or direct and QTM terms were employed, a suitable fitting pattern began to emerge. Ultimately,

10.1002/chem.202003556

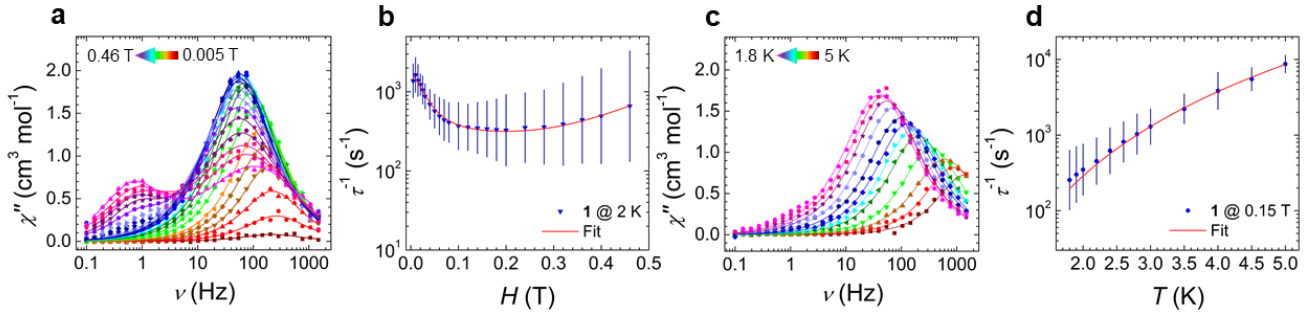

Figure 3. (a) Field-dependent ac magnetic susceptibility of **1**, performed at a constant temperature of 2 K; (b) field-dependent magnetic relaxation times, fit to a combination of Raman, direct, and quantum QTM terms; (c) frequency-dependent ac magnetic susceptibility data performed at a constant applied magnetic field of 0.15 T; (d) frequency-dependent magnetic relaxation times, fit to a single Raman relaxation mechanism, described in the main text.

it was only upon combining all three terms for Raman, direct, and QTM into the fitting equation that the most reasonable fits were obtained. The equation was used to fit the field dependent relaxation times (Figure 3b), with the following best fit output values of: C = 22.01 $K^{-3.65}$ s^{-1}, $C_1 = C_2 = 0$, n = 3.65, A = 4.30(81) x 10^3 K^{-1} T^{-4} s^{-1}, B_1 = 1331(58) s^{-1}, B_2 = 1192(200) T^{-2} (m = 4 for Kramers ion systems). The values of best fit for the Raman relaxation term from the field dependent data were used to fit the frequency-dependent relaxation times as well, with the value of n left variable to yield a value of n = 3.71. The direct and QTM terms were not employed in this fitting, as the applied magnetic field is not sufficient to activate the direct relaxation process which requires large fields, and the QTM is suppressed due to the application of a magnetic field which would overcome the quantum tunnelling relaxation pathway. While the values of n are not completely identical from one plot to the other, it is noted that the obtained fits still fall within the calculated error bars of the extracted relaxation times for both the field-dependent and frequency-dependent data sets. Due to this, it is reasonable to assess that compound **1** possesses slow magnetic relaxation when influenced by an external dc field, and experiences magnetic relaxation primarily through a Raman relaxation process.

Optical properties

Compound **1** features the typical near-infrared (NIR) emission of Yb^{3+} under UV-visible excitation (Figure 4). The diffuse reflectance spectrum (DRS) shows that **1** absorbs light up to approximately 680 nm. Considering the broad emission centred between 550 and 850 nm arising from the fluorescence of the ligands ($S_1 \rightarrow S_0$), the position of lowest singlet state S_1 (17240 cm^{-1}) was retrieved considering the intersection between the fluorescence band and the diffuse reflectance spectrum. Since the lowest singlet state of fod$^-$ lies above 30,000 cm^{-1},[38] the experimentally found S_1 should be attributed to the ring-opened tetrazine ligand. Admittedly, the extended absorption in the visible part of the spectrum can also result from charge transfer (CT) phenomena.[39] After absorption of the excitation light, sensitisation of Yb^{3+} emission can proceed through triplet state (T_1) population *via* intersystem crossing (ISC), followed by energy transfer (ET) to $^2F_{5/2}$ state of the lanthanide ion.[40,44] Another possibility is the occurrence of an internal redox process, as demonstrated in previous studies on Yb^{3+}-complexes.[41-45] This entails a ligand-to-metal CT (LMCT), resulting in a temporary reduction of the trivalent lanthanide to its divalent form, eventually leading to the population of the trivalent lanthanide ion excited state. Both pathways (ET- and CT-mediated sensitisation) are illustrated in Figure 4, where a tentative partial energy scheme of the compound is proposed. At this stage, the nature of Yb^{3+} sensitisation cannot be unambiguously discerned, but for the sake of the present discussion this is not a pivotal aspect of the studied system. In fact, regardless of the sensitisation mechanism involved, radiative relaxation from Yb^{3+} $^2F_{5/2}$ to the ground state ($^2F_{7/2}$) is observed in **1**. Interestingly, the main component of the $^2F_{5/2} \rightarrow {}^2F_{7/2}$ multiplet centred at approximately 10235 cm^{-1} is split in two (zoom-in Figure 4). This is indicative of the presence of two non-equivalent emission centres and is consistent with the different coordination environment of Yb1 and Yb2 (See Figure S1 and computational data).

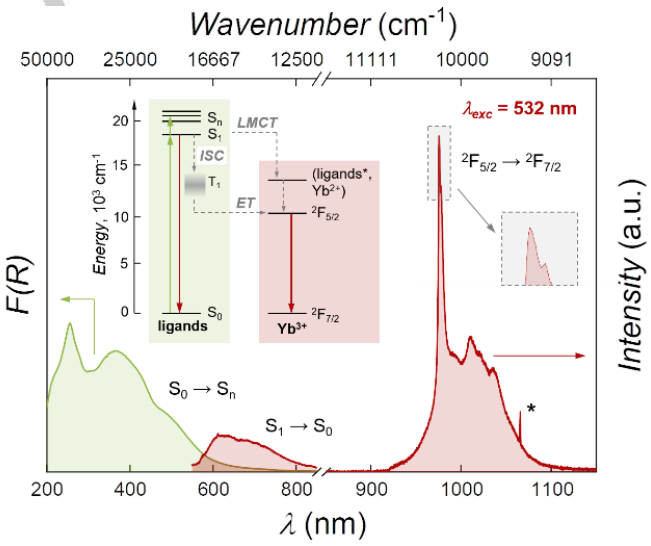

Figure 4. Diffuse reflectance spectrum (green line) along with the emission spectrum (red line) of **1**. The emission spectrum was recorded at 77 K. In the inset, the possible Yb^{3+} ligand-mediated sensitisation mechanisms are shown (upward solid lines – absorption; downward solid lines – emission; dashed lines – non-radiative processes; ET – energy transfer; ISC – intersystem crossing; LMCT – ligand-to-metal charge transfer). A spurious signal from the second harmonic of the excitation light (532 nm) appears around 1064 nm – marked with an asterisk. A zoom-in of the most intense $^2F_{5/2} \rightarrow {}^2F_{7/2}$ multiplet component is shown to better display its splitting in two components.

The luminescence properties of **1** can be harnessed to retrieve information regarding the energy level scheme. To that end, the comparison between the results obtained from spectroscopic measurements and theoretical modelling are reported below.

10.1002/chem.202003556

Theoretical calculations

To obtain proper description of the splitting of energy levels of **1** and to investigate its magnetic properties computationally, we carried out multiple CASSCF/(XMS-CASPT2)//SO-RASSI[46-53] calculations for the smaller model system **A** and its fragments (**B-F**) that were constructed from the crystal structure of **1** (Figure S8). The omission of fluorinated backbones of fod$^-$ ligands in the model system **A** might influence the calculated energy spectrum and magnetic properties of **1** because electronegative fluorine atoms in the proximity of coordinating atoms influence on the electron density distribution around metal centre that further has an small effect the energy spectra and magnetic properties of investigated systems as previously reported for dinuclear Dy- and Tb-complexes with similar type fluorinated acac ligands.[54,55] However, trimming down the size of **1** is required because the XMS-CASPT2 calculations are not computationally feasible for **1** due to its large size but necessary to model the dynamic electron correlation effects outside of 4f orbital space that heavily influence on the splitting of the energy levels of ytterbium complexes.[6,54,56-60] Nonetheless, the validity of our model systems and chosen computational approach can be benchmarked against the experimental energy spectrum of **1** obtained from the emission measurements (Figure 5). Previous CASSCF calculations carried out for large magnetic metal clusters have also shown that any fragmentation of clusters might lead to the erroneous results when the calculated magnetic properties of clusters are investigated.[61] Therefore, and in order to obtain the smallest plausible systems for the final CASSCF/XMS-CASPT2//SO-RASSI calculations, we first systematically investigated the influence of fragmentation on the relative splitting of energy levels of **1** using the CASSCF//SO-RASSI method with a smaller basis (Basis1) set followed by the CASSCF/(XMS-CASPT2)//SO-RASSI calculations with larger basis sets (Basis2 and Basis3) only for the most promising fragment. Due to the inversion symmetry of **1**, all calculations were carried only for two symmetrically inequivalent Yb1 and Yb2 ions.

The detailed discussion and results of fragment calculations is given in the ESI and Tables S10 and S11, and they outlined the suitability of the fragment **B** in conjunction with smaller basis set (Basis3) for the most demanding CASSCF/XMS-CASPT2//SO-RASSI/Basis3 calculations as well as the importance of dynamic electron correlation effects through the XMS-CASPT2 method to correctly describe the splitting of the energy levels of Yb^{3+} ions. Indeed, for Yb1, the CASSCF/XMS-CASPT2//SO-RASSI/Basis3 values for the first, second, and third excited KDs are 404.4 cm^{-1}, 484.5 cm^{-1}, and 607.1 cm^{-1}, whereas for Yb2, the same values are 380.1 cm^{-1}, 549.6 cm^{-1}, and 661.7 cm^{-1}. Comparing these calculated values to the experimental data from spectroscopic analysis (348 cm^{-1}, 468 cm^{-1}, and 598 cm^{-1}), it can be concluded that all other calculated values are in agreement with the experimental data, except the calculated values for the second and third excited KDs of Yb2 ion that are 81.6 cm^{-1} and 63.7 cm^{-1} higher in energy than their corresponding experimental values. It cannot be unambiguously concluded if the discrepancies between experimental and computational data arise from the improper model system (omission of fluorine substitution) because the results of the calculations could also indicate that **1** has two spectroscopically and magnetically distinct Yb^{3+} ions (*vide infra*). This assumption is supported by observation of the experimental

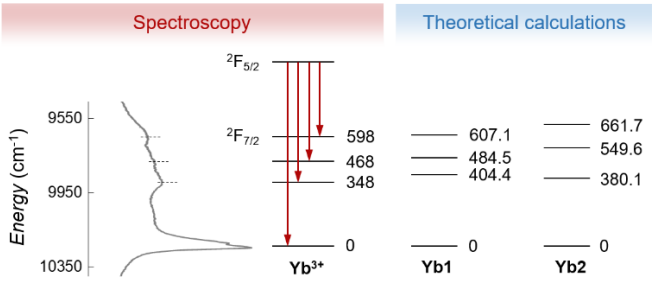

Figure 5. Comparison of the position of the four $^2F_{7/2}$ KDs obtained from the analysis of the luminescence spectrum ($^2F_{5/2} \rightarrow {}^2F_{7/2}$) and theoretical calculations carried out at the CASSCF/XMS-CASPT2//SO-RASSI/Basis3 level for the fragment **B**. Horizontal dashed lines in the luminescence spectrum are drawn in correspondence of the $^2F_{5/2} \rightarrow {}^2F_{7/2}$ multiplet components.

emission spectrum of **1**. In fact, the most intense component of the $^2F_{5/2} \rightarrow {}^2F_{7/2}$ multiplet is composed of two closely spaced sharp peaks centred respectively at 10248 and 10223 cm^{-1}, which likely arise from two non-equivalent Yb^{3+} ions (Figure 4). Moreover, the presence of two maxima in the field dependence measurements of χ'' might indicated the presence of two distinct magnetic centres in **1** although two different maxima showing either temperature or field dependence or both can also originate from the sufficiently wide dipolar field distribution in the sample.[62] The dipolar field can create two distinct domains of the total magnetic interaction where either QTM, direct, or Raman process dominates each other at low temperature regime. The large energy gaps between the ground and the first excited KDs observed for both distinct Yb^{3+} ions along with the fact that Orbach process does not play a role in the slow relaxation of the magnetisation of **1** support the latter explanation, whereas the small calculated intramolecular dipolar coupling constants (less than -0.1 cm^{-1}, Table S5) between Yb^{3+} ions in **1** support the first explanation; as the dipolar interaction is inversely proportional to the cubic of distance between two magnetic centres and the shortest intermolecular distance between Yb^{3+} ions is ~ 12 Å in **1**, it can be estimated that the magnitudes of the intermolecular dipolar interactions in **1** are smaller than the magnitude of intramolecular interactions, and thus, they should not generate a very strong dipolar field in the sample.

Further insight for the magnetic properties of **1** was obtained by extracting them from the CASSCF/XMS-CASPT2//SO-RASSI/Basis3 wavefunction of **B**. The main magnetic axes of Yb^{3+} ions in **1** are slightly oriented away from the plane formed by the four Yb^{3+} ions as depicted in Figure S9. For both distinct Yb^{3+} ions the magnetic axes of the three excited KDs of $^2F_{7/2}$ ground state are clearly tilted away from the main magnetic axis of the ground state highlighting the low magnetic axiality of both Yb^{3+} ions (Tables S12 and S13). The low axiality of both ions is also evident from the calculated **g**-tensors of the KDs. Although the g_z values of ground KDs (g_z = 7.365 for Yb1; g_z = 7.826 for Yb2) of Yb1 and Yb2 indicate a relatively strong axiality for both ions, they have also non-negligible transverse components in their **g**-tensors (g_x = 0.387 g_y = 0.444, g_z = 7.365 for Yb1; g_x = 0.116 g_y = 0.205, g_z = 7.826 for Yb2) that suppress the axiality. Even though the calculated transverse components of ground KDs are relatively small compared to the values reported for other Yb complexes,[9,57,59,63] in which Yb ions reside in low symmetry coordination environments, they are large enough to facilitate the

QTM in the ground Kramers doublet. Indeed, the inspection of transition moment matrix elements between different electronic states reveal substantial tunnelling probability within the ground KDs for both Yb^{3+} ions (Figure S10). The result is fully in line with experimental ac measurements without the applied dc field. For both Yb^{3+} ions, the axiality of excited KDs is clearly lower than the axiality of the ground KD as illustrated with the calculated values of their **g**-tensors (Tables S12 and S13).

The percentage decompositions of the CASSCF/XMS-CASPT2//SO-RASSI/Basis3 wavefunctions of Yb1 and Yb2 are presented in Table S14 and Table S15, respectively. Interestingly, the ground KD of Yb2 ion, can be described almost as a pure M_J = ± 7/2 state that has only minor components from the other M_J states. Such a pure M_J = ± 7/2 state has been observed before for Yb^{3+} ion,[9] but usually Yb^{3+} ions in the low symmetry coordination environment have more mixed ground KD.[56,59] This is indeed observed for Yb1; its ground KD cannot be assigned to any pure M_J as it composed of several M_J state with varying contributions. All the excited KD of both Yb^{3+} ions show stronger mixing than their ground states.

The slightly differing energy spectra, **g**-tensors, and percentage decomposition of the CASSCF/XMS-CASPT2//SO-RASSI/Basis3 wavefunctions of Yb1 and Yb2 ions, can be rationalized by analysing the effective charges of coordinating atoms that were calculated with the LoProp program[64] for the fragment **B** at the CASSCF/XMS-CASPT2//SO-RASSI/Basis3 level of theory. The effective charges of coordinating O atoms around Yb1 and Yb2 ions vary from -0.90 to -0.99, whereas the effective charges of coordinating N atoms are less than -0.50, expect the effective charge of N4 that is -0.75 (Table S16). The calculated effective charges imply that the equatorially coordinated O1, O2 and N4 atoms around Yb1 effectively compensate the crystal ligand field generated by four O atoms (O3-O6) of two fod^- ligands on the axial positions of Yb1. Contrast to Yb1, Yb2 has only one O atom (O11) on its equatorial positions while other three equatorial positions are occupied with softer N atoms (N1, N2, N6) having smaller effective charges than four O atoms (O7-O10) occupying the axial positions of Yb2. Thus, Yb1 is less axial than Yb2 although both ions reside in the distorted square antiprism geometry. Indeed, the calculated **g**-tensors of ground KDs of Yb1 and Yb2 illustrate well the higher axiality of Yb2 over Yb1 (see above).

In sum, the calculated magnetic properties and energy spectra for the fragment **B** support the experimental findings well for three reasons. First, the computational data proof that Yb^{3+} ions in **1** are weakly magnetically coupled to each other that is evident from the experimental χT plot that do not show any significant sharp decrease (increase) at low temperatures that usually originates from strong antiferromagnetic (ferromagnetic) coupling between magnetic centres. Second, the QTM is one of the main relaxation pathways for the relaxation of the magnetisation in **1** without the applied dc field as illustrated with the calculated non-negligible transverse components of the **g**-tensors of the ground KDs and the non-negligible values of the transition moment matrix elements within ground KDs. Third, calculations proof that Yb1 and Yb2 ions have slightly different magnetic properties and energy spectra due to the dissimilar distribution of the coordinating atoms within their distorted square antiprism coordination environments. The last finding support the fact that the two closely spaced sharp peaks at 10248 and 10223 cm^{-1} observed in the emission spectrum of **1** arise from the most intense component of the $^2F_{5/2} \rightarrow {}^2F_{7/2}$ multiplet of two non-equivalent Yb^{3+} ions.

Conclusion

Through magnetic and luminescence experiments, coupled with theoretical calculations, a detailed analysis of a new [Yb_4] complex has been performed. The initial employment of the ligand bpztz lead to the unexpected isolation of the ring-opened compound **1**, which is formed through the presence of two bpzch molecules. The utilisation of the Kramers ion Yb^{3+} led to compound **1** exhibiting both photoluminescence as well as slow magnetic relaxation upon application of a magnetic field. This behaviour was further confirmed through extensive computational studies. The QTM exhibited in the absence of an applied dc field was justified through the presence of non-negligible transverse components of the **g**-tensors. Furthermore, the excited KDs of the Yb centres, particularly the excited KDs of Yb1, closely match between the luminescence measurements and *ab initio* calculations when all subtle electron correlation effects were taken into account in the calculations. Experimental and computational data showed also that **1** contains two distinct Yb^{3+} ions with slightly different energy spectra and magnetic properties. The presented results not only the highlight a system in which two different physical properties are incorporated into the one molecule, but also underline how reactions conditions could lead to unexpected ligand transformation and unique coordination compounds.

Experimental Section

Materials

3,6-dipyrazin-2-yl-1,2,4,5-tetrazine (bpztz) was synthesized using a previously reported method.[65] $Yb(fod)_3$ (fod^- = 6,6,7,7,8,8,8-heptafluoro-2,2-dimethyl-3,5-octanedionate) and $CoCp_2$ (Cp^- = cyclopentadiene) were purchased from Strem Chemicals and used without further purification. All manipulations were performed in a nitrogen-filled glovebox. Solvents were dried using alumina-columns in a J.C. Meyer solvent system, degassed with multiple freeze-pump-thaw cycles, and stored over 4Å molecular sieves.

Synthesis of $[Yb_4(bpzch)_2(fod)_{10}]$ (1)

In a nitrogen-filled glovebox, bpztz (30 mg, 0.125 mmol), $Yb(fod)_3$ (269 mg, 0.250 mmol) and $CoCp_2$ (24 mg, 0.125 mmol) were weighed into three separate vials. 2 mL of benzene was added to each vial, and the vials were stirred for five minutes. The vial containing the solution of $CoCp_2$ was added to the vial containing bpztz, and the previously red solution turned dark purple in colour after stirring for one minute. To this mixture was added the vial containing the $Yb(fod)_3$ solution, and the resulting mixture was stirred for an additional minute, then left to sit for 5 minutes. The clear, dark brown solution on top was decanted from the resulting solid and placed in a -30 °C freezer. Dark orange crystals suitable for single-crystal X-ray analysis formed after a week. Yield = 8.15%. Elemental analysis; calculated: C, 35.17; H, 2.80; N, 4.10; found: C, 35.25; H, 2,77; N, 5.26. IR (ATR, cm^{-1}): 2967 (m), 1621

(s), 1549 (w), 1508 (m), 1466 (m) 1395 (w), 1367 (w), 1345 (m), 1259 (w), 1220 (s), 1155 (s), 1105 (s), 1067 (s), 1020 (s), 966 (m), 939 (w), 908 (m), 870 (w), 793 (s), 752 (w), 740 (w), 688 (m), 629 (w), 596 (w).

Physical measurements

Infrared analysis was performed with a Nicolet 6700 FT-IR spectrometer equipped with an ATR from 4000 – 500 cm^{-1}. Elemental analysis was performed using a vario Isotope Cube equipped with an autosampler.

Single-crystal X-ray diffraction studies

Single crystals of **1** suitable for X-ray diffraction studies were mounted on a thin glass fibre using paraffin oil.

Magnetic measurements

Magnetic measurements were performed using a Quantum Design SQUID MPMS-XL7 magnetometer, using temperature ranges of 1.8 to 300 K and applied fields of 0 to 7 T. Direct current (dc) magnetic susceptibility measurements were performed on a polycrystalline sample of **1** (26 mg) which was anchored in grease and wrapped in a polyethylene membrane. Magnetisation data was collected at 100 K as a check for ferromagnetic impurities in the sample (Figure S11). Diamagnetic corrections were applied for the sample holder and polyethylene membrane, and the intrinsic diamagnetism of the sample was estimated using Pascal's constants. Alternating current (ac) magnetic susceptibility measurements were performed in a temperature range of 1.8 to 5 K, under an applied dc field of 0.08 T.

Photoluminescence studies

The diffuse reflectance spectrum was recorded on a Cary Varian 5000 in the 200-850 nm range with a scan step of 1 nm and a scan speed of 600 nm min^{-1} equipped with an accessory for solid-state measurements. Photoluminescence measurements were performed on a homemade setup. The powdered sample was placed in a 2-mm-deep copper holder, covered with a glass slip and mounted on a copper disk in a liquid nitrogen-cooled cryostat. The spectra were recorded in the visible range with a Horiba Scientific Symphony Silicon CCD Detector 1024x256 (Horiba, New Jersey, USA) and in the near-infrared range with a Horiba Scientific Symphony 1700 InGaAs CCD Detector 1024x256 (Horiba, New Jersey, USA). The sample was kept at 77 K, excited with a 532 nm 300 mW quantum well diode laser (M Series, Dragon lasers, China) and focusing the excitation beam on the sample with a 5 cm focus length lens (power density on the sample was approximately 1 W cm^{-2}). The PL emission signal was collected at 180°, through the same objective lens, and the excitation light was filtered off using a long-pass filter (> 550 nm).

Computational details

The geometry of model system **A** and fragments **B**-**F** were extracted from the crystal structure of **1**. Before any CASSCF [46-48] and broken symmetry density function theory (BS-DFT)[66-69] calculations were performed, the positions of hydrogen atoms were optimized at the RI-PBE-D3/def2-TZVP[70-78] level of theory using the Turbomole program package,[79] while the positions of heavier atoms were fixed to the coordinates of crystal structure. In this initial optimisation step, Yb^{3+} ions were replaced with Y^{3+} ions to avoid convergence problems. The effective core potential was used for the core electrons of Y^{3+} ions.[80]

To calculate the energy spectrum and magnetic properties of **1**, the CASSCF/(XMS-CASPT2)//SO-RASSI[46-53] calculations were performed for the model system **A** and its fragments **B**-**F** in conjunction with three different ANO-RCC type basis sets (Table S9).[81,82] All CASSCF/(XMS-CASPT2)//SO-RASSI calculations were carried out with the MOLCAS quantum chemistry program package version 8.2.[83] Due the inversion symmetry of **1**, the CASSCF calculations were done independently for both symmetrically inequivalent Yb1 and Yb2 ions while others Yb^{3+} ions were replaced with Lu^{3+} ions. The scalar relativistic effects were modelled using the exact two component (X2C) transformation[50,84,85] and Cholesky decomposition with the threshold value of 10^{-8} was employed in two electron integrals calculations to speed up the calculations. In all state-averaged CASSCF calculations all 7 doublets arising from the active space of 13 electrons and 7 4f-orbitals of Yb^{3+} ions were solved. The dynamic electron correlation effects were calculated on top of the spin-free CASSCF wave functions without the mixing of the CASSCF eigenstates under dynamic electron correlation employing XMS-CASPT2 approach.[52,53] The XMS-CASPT2 variant was chosen over the conventional CASPT2[50,51] method because it is a less prone for the artificial splitting of spatially degenerate states than the conventional method.[53] All spin-free states obtained either from the state-averaged CASSCF or XMS-CASPT2 calculations were mixed by spin-orbit coupling using the restricted active space state interaction (SO-RASSI) approach to obtain final energy spectra and wave functions of both Yb^{3+} ions.[53] The static magnetic properties of Yb1 and Yb2 were extracted from the final SO-RASSI wave functions using the SINGLE_ANISO routine,[86-90] whereas the magnetic exchange and dipolar interactions between Yb^{3+} ions were calculated with the POLY_ANISO routine.[87,88] The Lines model,[91] as implemented in the POLY_ANISO routine, was used to model the exchange interactions with the following Heisenberg Hamiltonian:

$$\hat{H}_{ij}^{exch} = -\sum_{i \neq j} J_{ij}^{exch} \hat{S}_i \cdot \hat{S}_j \quad (3)$$

where J_{ij}^{exch} is the exchange coupling constant between interacting Yb^{3+} sites *i* and *j*, and $\hat{S}_i$ and $\hat{S}_j$ are the local spin-operators (S=1/2) of these two interacting sites in the absence of spin-orbit coupling. The four modelled exchange coupling constants are visualized in Figure S9. Initial guesses for the exchange coupling constants were obtained from the BS-DFT calculations (see ESI), and their final values were obtained by fitting the calculated susceptibility and magnetisation data to the experimental data. In the fitting procedure, 2 spin-orbit states were included from each Yb^{3+} centres into the exchange interaction and dipolar interactions were calculated as implemented in the POLY_ANISO routine; the resulting exchange energy spectrum is given in Table S17 and the calculated χT and M plots are illustrated in Figure 2 and S3, respectively. It should be pointed out that although the shape of χT and M plots were reproduced very well by calculations, the calculated values of χT and M needed to be scaled up by 4.8% and 6.5%, respectively, to get quantitative agreement between the experimental and calculated data. Because dynamic electron correlation effects were taken properly into account in *ab initio* calculations, the

discrepancies between experimental and calculated data can arise from the improper model system (omission of the fluorine substituents), plausible mixing of Yb^{2+}/Yb^{3+} states in the ground state wave function of **1** and/or a small diamagnetic impurity in the sample. Similar discrepancies between experimental and calculated χT and M data have also been reported for other Yb based single-molecule magnets before and their origins have remained elusive.[57,92,93]

In order to evaluate the total magnetic interactions ($\tilde{J}_{ij}^{exch} + \tilde{J}_{ij}^{dip} = \tilde{J}_{ij}^{total}$) between Yb^{3+} ions, the obtained Lines exchange coupling constants were converted to the non-collinear Ising exchange parameters using equation 4:

$$\tilde{J}_{ij}^{exch} = J_{ij}^{exch} cos\varphi_{ij} \qquad (4)$$

in which φ_{ij} is the angle between the main anisotropy axes of the interacting sites *i* and *j*.[94] The dipolar coupling constants were also calculated through non-collinear Ising model:

$$\tilde{J}_{ij}^{dip} = \mu_B^2 g_{zi} g_{zj} \frac{cos\theta_{ij} - 3cos\theta_{in} cos\theta_{jn}}{r^3}, \quad (5)$$

where μ_B is the Bohr magneton, g_{zi} (g_{zj}) is the z-component of **g**-tensor of the *i*th (*j*th) centre obtained from the CASSCF/XMS-CASPT2//SO-RASSI/Basis 3 calculation, r is the distance between two Yb^{3+} ions, and θ_{ij} is the angle between the main magnetic axes of the *i*th and *j*th centres, whereas θ_{in} (θ_{jn}) is the angle between the main magnetic axis of *i*th (*j*th) centre and the vector connecting two interacting Yb^{3+} ions.[95] If one considers the values of the **g**-tensors of the ground KDs of Yb1 and Yb2 ions, it can be concluded that the employed Ising approximation holds sufficiently enough for both Yb^{3+} centres.

Acknowledgements

The authors would like to acknowledge the financial support provided by the University of Ottawa, the Natural Sciences and Engineering Research Council of Canada (NSERC), and the Academy of Finland (projects 315829, 320015). P.R. would like to thank the Government of Ontario for an Ontario Graduate Scholarship (OGS). CSC-IT Centre for Science in Finland, the Finnish Grid and Cloud Infrastructure (persistent identifier urn:nbn:fi:research-infras-2016072533) and Prof. H. M. Tuononen (University of Jyväskylä) are acknowledged for providing computational resources for the project.

Keywords: ytterbium • single-molecule magnets • opto-magnetic properties • photoluminescence • tetrazine

References

[1] C. A. P. Goodwin, F. Ortu, D. Reta, N. F. Chilton and D. P. Mills, *Nature* **2017**, *548*, 439-442.

[2] F.-S. Guo, B. M. Day, Y.-C. Chen, M.-L. Tong, A. Mansikkamäki and R. Layfield, *Science* **2018**, *362*, 1400-1403.

[3] D. Errulat, R. Marin, D. A. Gálico, K. L. M. Harriman, A. Pialat, B. Gabidullin, F. Iikawa, O. D. D. Couto Jr., J. O. Moilanen, E. Hemmer, F. A. Sigoli, M. Murugesu, *ACS Cent. Sci.* **2019**, *5*, 1187-1198.

[4] A. Skripka, A. Benayas, R. Marin, P. Canton, E. Hemmer, F. Vetrone, *Nanoscale* **2017**, *9*, 3079-3085.

[5] F. Pointillart, B. Le Guennic, S. Golhen, O. Cador, O. Maury, L. Ouahab, *Chem. Commun.* **2013**, *49*, 615-617.

[6] A. B. Castro, J. Jung, S. Golhen, B. Le Guennic, L. Ouahab, O. Cador, F. Pointillart, *Magnetochemistry* **2016**, *2*, 26.

[7] J. D. Hilgar, M. G. Bernbeck, J. D. Rinehart, *J. Am. Chem. Soc.* **2019**, *141*, 1913-1917.

[8] M.-M. Wang, X.-Q. Wei, J.-L. Zhu, J. Wang, M. Wang, L.-Z. Liu, T.-M. Sun, Y.-F. Tang, *J. Solid State Chem.* **2020**, *283*, 121172.

[9] G. Brunet, R. Marin, M.-J. Monk, U. Resch-Genger, D. A. Gálico, F. A. Sigoli, E. A. Suturina, E. Hemmer, M. Murugesu, *Chem. Sci.* **2019**, *10*, 6799-6808.

[10] J. Wang, J. J. Zakrzewski, M. Heczko, M. Zychowicz, K. Nakagawa, K. Nakabayashi, B. Sieklucka, S. Chorazy, S. Ohkoshi, *J. Am. Chem. Soc.* **2020**, *142*, 3970-3979.

[11] J. Long, M. S. Ivanov, V. A. Khomchenko, E. Mamontova, J.-M. Thibaud, J. Rouquette, M. Beaudhuin, D. Granier, R. A. S. Ferreira, L. D. Carlos, B. Donnadieu, M. S. C. Henriques, J. A. Paixão, Y. Guari, J. Larionova, *Science* **2020**, *367*, 671-676.

[12] D. I. Alexandropoulos, K. R. Vignesh, T. C. Stamatatos, K. R. Dunbar, *Chem. Sci.* **2019**, *10*, 1626-1633.

[13] P. Chábera, Y. Liu, O. Prakash, E. Thyrhaug, A. El Nahhas, A. Honarfar, S. Essén, L. A. Fredin, T. C. B. Harlang, K. S. Kjær, K. Handrup, F. Ericson, H. Tatsuno, K. Morgan, J. Schnadt, L. Häggström, T. Ericsson, A. Sobkowiak, S. Lidin, P. Huang, S. Styring, J. Uhlig, J. Bendix, R. Lomoth, V. Sundström, P. Persson, K. Wärnmark, *Nature* **2017**, *543*, 695-699.

[14] T. Okubo, K. Himoto, K. Tanishima, S. Fukuda, Y. Noda, M. Nakayama, K. Sugimoto, M. Maekawa, T. Kuroda-Sawa, *Inorg. Chem.* **2018**, *57*, 2373-2376.

[15] X.-H. Bu, H. Liu, M. Du, L. Zhang, Y.-M. Guo, *Inorg. Chem.* **2002**, *41*, 1855-1861.

[16] S. Patra, T. A. Miller, B. Sarkar, M. Niemeyer, M. D. Ward, G. K. Lahiri, *Inorg. Chem.* **2003**, *42*, 4707-4713.

[17] A. Dogan, B. Schwederski, T. Schleid, F. Lissner, J. Fiedler, W. Kaim, *Inorg. Chem. Commun.* **2004**, *7*, 220-223.

[18] S. Maji, B. Sarkar, S. Patra, J. Fiedler, S. M. Mobin, V. G. Puranik, W. Kaim, G. K. Lahiri, *Inorg. Chem.* **2006**, *45*, 1316-1325.

[19] M. A. Lemes, A. Pialat, S. N. Steinmann, I. Korobkov, C. Michel, M. Murugesu, *Polyhedron* **2016**, *108*, 163-168.

[20] M. A. Lemes, H. N. Stein, B. Gabidullin, S. N. Steinmann, M. Murugesu, *ACS Omega* **2018**, *3*, 10273-10277.

[21] M. Takahashi, H. Kikuchi, *Tetrahedron Lett.* **1987**, *28*, 2139-2142.

[22] S. Goswami, H. S. Jena, S. Konar, *Inorg. Chem.* **2014**, *53*, 7071-7073.

[23] T. J. Woods, M. F. Ballesteros-Rivas, S. M. Ostrovsky, A. V. Palii, O. S. Reu, S. I. Klokishner, K. R. Dunbar, *Chem. Eur. J.* **2015**, *21*, 10302-10305.

[24] D. I. Alexandropoulos, B. S. Dolinar, K. R. Vignesh, K. R. Dunbar, *J. Am. Chem. Soc.* **2017**, *139*, 11040-11045.

[25] M. A. Lemes, H. N. Stein, B. Gabidullin, K. Robeyns, R. Clérac, M. Murugesu, *Chem. Eur. J.* **2018**, *24*, 4259-4263.

[26] B. Li, X.-N. Wang, A. Kirchon, J.-S. Qin, J.-D. Pang, G.-L. Zhuang, H.-C. Zhou, *J. Am. Chem. Soc.* **2018**, *140*, 14581-14585.

[27] N. S. Oxtoby, A. J. Blake, N. R. Champness, C. Wilson, *Proc. Nat. Acad. Sci.* **2002**, *99*, 4905-4910.

[28] N. S. Oxtoby, A. J. Blake, N. R. Champness, C. Wilson, *Dalton Trans.* **2003**, 3838-3839.

[29] B. Sarkar, W. Kaim, T. Schleid, I. Hartenbach, J. Fiedler, *Z. Anorg. Allg. Chem.* **2003**, *629*, 1353-1357.

[30] D. Casanova, M. Llunell, P. Alemany, S. Alvarez, *Chem. Eur. J.* **2005**, *11*, 1479-1494.

[31] F. Pointillart, O. Cador, B. Le Guennic, L. Ouahab, *Coord. Chem. Rev.* **2017**, *346*, 150-175.

[32] M.-M. Wang, X.-Q. Wei, J.-L. Zhu, J. Wang, M. Wang, L.-Z. Liu, T.-M. Sun, Y.-F. Tang, *J. Solid State Chem.* **2020**, *283*, 121172.

[33] P. Richardson, D. A. Gálico, J. Ovens, F. A. Sigoli, M. Murugesu, *Dalton Trans.* **2020**, DOI: 10.1039/D0DT00696C.

[34] M. Fondo, J. Corredoira-Vázquez, A. M. Garcia-Deibe, J. Sanmartin Matalobos, M. Amoza Dávila, A. Botas, R. Ferreira, L. A. D. Carlos, E. Colacio, *Inorg. Chem. Front.* **2020**, DOI: 10.1039/D0QI00637H.

[35] W. Chen, L. Zhong, Y. Zhong, Y. Zhang, S. Gao, W. Dong, *Inorg. Chem. Front.*, **2020**, DOI: 10.1039/D0QI00628A.
[36] D. Reta, N. Chilton, *Phys. Chem. Chem. Phys.* **2019**, *21*, 23567-23575.
[37] K. N. Shrivastava, *Phys. Status Solidi B* **1983**, *117*, 437-458.
[38] A. D'Aléo, A. Picot, A. Beeby, J. A. G. Williams, B. Le Guennic, C. Andraud, O. Maury, *Inorg. Chem.* **2008**, *47*, 10258-10268.
[39] R. Xiong, D. Mara, J. Liu, R. Van Deun, K. E. Borbas, *J. Am. Chem. Soc.* **2018**, *140*, 10975-10979.
[40] Y.-J. Huang, C. Ke, L.-M. Fu, Y. Li, S.-F. Wang, Y.-C. Ma, J.-P. Zhang, Y. Wang, *ChemistryOpen* **2019**, *8*, 388-392.
[41] W. D. Horrocks, J. P. Bolender, W. D. Smith, R. M. Supkowski, *J. Am. Chem. Soc.* **1997**, *119*, 5972-5973.
[42] M. D. Ward, *Coord. Chem. Rev.* **2010**, *254*, 2634-2642.
[43] E. Di Piazza, L. Norel, K. Costuas, A. Bourdolle, O. Maury, S. Rigaut, *J. Am. Chem. Soc.* **2011**, *133*, 6174-6176.
[44] M. Feng, F. Pointillart, B. Le Guennic, B. Lefeuvre, S. Golhen, O. Cador, O. Maury, L. Ouahab, *Chem. Asian J.* **2014**, *9*, 2814-2825.
[45] J.-C. G. Bünzli, *Coord. Chem. Rev.* **2015**, *293-294*, 19-47.
[46] P. Siegbahn, A. Heiberg, B. Roos, B. Levy, *Phys. Scr.* **1980**, *21*, 323–327.
[47] B. O. Roos, P. R. Taylor, P. E. M. Sigbahn, *Chem. Phys.* **1980**, *48*, 157–173.
[48] B. O. Roos, R. Lindh, P. Å. Malmqvist, V. Veryazov, P.-O. Widmark, *Multiconfigurational Quantum Chemistry*, John Wiley & Sons, Inc., Hoboken, NJ, USA, **2016**.
[49] P. Å. Malmqvist, B. O. Roos, B. Schimmelpfennig, *Chem. Phys. Lett.* 1**2002**, *357*, 230–240.
[50] D. Peng, M. Reiher, *Theor. Chem. Acc.* **2012**, *131*, 1081.
[51] K. Andersson, P. Å. Malmqvist, B. O. Roos, A. J. Sadlej, K. Wolinski, *J. Phys. Chem.* **1990**, *94*, 5483–5488
[52] T. Shiozaki, W. Győrffy, P. Celani, H.-J. Werner, *J. Chem. Phys.* **2011**, *135*, 081106.
[53] A. A. Granovsky, *J. Chem. Phys.* **2011**, *134*, 214113.
[54] F. Pointillart, J. Jung, R. Berraud-Pache, B. Le Guennic, V. Dorcet, S. Golhen, O. Cador, O. Maury, Y. Guyot, S. Decurtins, et al., *Inorg. Chem.* **2015**, *54*, 5384–5397.
[55] D. A. Gálico, R. Marin, G. Brunet, D. Errulat, E. Hemmer, F. A. Sigoli, J. O. Moilanen, M. Murugesu, *Chem. Eur. J.* **2019**, *25*, 14625-14637.
[56] F. Guégan, J. Jung, B. Le Guennic, F. Riobé, O. Maury, B. Gillon, J.-F. Jacquot, Y. Guyot, C. Morell, D. Luneau, *Inorg. Chem. Front.* **2019**, *6*, 3152–3157.
[57] G. Cosquer, F. Pointillart, J. Jung, B. Le Guennic, S. Golhen, O. Cador, Y. Guyot, A. Brenier, O. Maury, L. Ouahab, *Eur. J. Inorg. Chem.* **2014**, *2014*, 69–82.
[58] A. Belio Castro, J. Jung, S. Golhen, B. Le Guennic, L. Ouahab, O. Cador, F. Pointillart, *Magnetochemistry* **2016**, *2*, 26.
[59] J. Jung, T. T. da Cunha, B. Le Guennic, F. Pointillart, C. L. M. Pereira, J. Luzon, S. Golhen, O. Cador, O. Maury, L. Ouahab, *Eur. J. Inorg. Chem.* **2014**, *2014*, 3888–3894.
[60] N. A. G. Bandeira, C. Daniel, A. Trifonov, M. J. Calhorda, *Organometallics* **2012**, *31*, 4693–4700.
[61] M. Perfetti, J. Rinck, G. Cucinotta, C. E. Anson, X. Gong, L. Ungur, L. Chibotaru, M.-E. Boulon, A. K. Powell, R. Sessoli, *Front. Chem.* **2019**, *7*, 1–8.
[62] L. T. A. Ho, L. F. Chibotaru, *Phys. Rev. B,* **2018**, *98*, 174418.
[63] P.-H. Lin, W.-B. Sun, Y.-M. Tian, P.-F. Yan, L. Ungur, L. F. Chibotaru, M. Murugesu, *Dalton Trans.* **2012**, *41*, 12349.
[64] L. Gagliardi, R. Lindh, G. Karlström, *J. Chem. Phys.* **2004**, *121*, 4494-4500.
[65] W.-X. Hu, G.-W. Rao, Y.-Q. Sun, *Bioorg. Med. Chem. Lett.* **2004**, *14*, 1177-1181.
[66] W. Koch, M. C. Holthausen, *A Chemist's Guide to Density Functional Theory*, Wiley-VCH Verlag GmbH, Weinheim, FRG, **2001**.
[67] L. Noodleman, J. G. Norman, J. H. Osborne, A. Aizman, D. A. Case, *J. Am. Chem. Soc.* **1985**, *107*, 3418–3426.
[68] L. Noodleman, *J. Chem. Phys.* **1981**, *74*, 5737–5743.
[69] L. Noodleman, E. R. Davidson, *Chem. Phys.* **1986**, *109*, 131–143.
[70] K. Eichkorn, O. Treutler, H. Öhm, M. Häser, R. Ahlrichs, *Chem. Phys. Lett.* **1995**, *240*, 283–290.
[71] K. Eichkorn, O. Treutler, H. Öhm, M. Häser, R. Ahlrichs, *Chem. Phys. Lett.* **1995**, *242*, 652–660.
[72] K. Eichkorn, F. Weigend, O. Treutler, R. Ahlrichs, *Theor. Chem. Accounts Theory, Comput. Model. (Theoretica Chim. Acta)* **1997**, *97*, 119–124.
[73] J. P. Perdew, Y. Wang, *Phys. Rev. B* **1992**, *45*, 13244–13249.
[74] J. J. Perdew, K. Burke, M. Ernzerhof, *Phys. Rev. Lett.* **1996**, *77*, 3865–3868.
[75] S. Grimme, S. Ehrlich, L. Goerigk, *J. Comput. Chem.* **2011**, *32*, 1456–1465.
[76] S. Grimme, J. Antony, S. Ehrlich, H. Krieg, *J. Chem. Phys.* **2010**, *132*, 154104.
[77] F. Weigend, R. Ahlrichs, *Phys. Chem. Chem. Phys.* **2005**, *7*, 3297–3305.
[78] F. Weigend, *J. Comput. Chem.* **2008**, *29*, 167–175.
[79] TURBOMOLE V7.3 2018, a development of University of Karlsruhe and Forschungszentrum Karlsruhe GmbH, 1989-2007, TURBOMOLE GmbH, since 2007; available from http://www.turbomole.com.
[80] D. Andrae, U. Haeussermann, M. Dolg, H. Stoll, H. Preuss, *Theor. Chim. Acta* **1990**, *77*, 123–141.
[81] B. O. Roos, R. Lindh, P.-Å. Malmqvist, V. Veryazov, P.-O. Widmark, A. C. Borin, *J. Phys. Chem. A* **2008**, *112*, 11431–11435.
[82] B. O. Roos, R. Lindh, P.-\rAke Malmqvist, V. Veryazov, P.-O. Widmark, *J. Phys. Chem. A* **2004**, *108*, 2851–2858.
[83] F. Aquilante, J. Autschbach, R. K. Carlson, L. F. Chibotaru, M. G. Delcey, L. De Vico, I. Fdez. Galván, N. Ferré, L. M. Frutos, L. Gagliardi, et al., *J. Comput. Chem.* **2016**, *37*, 506–541.
[84] M. Filatov, *J. Chem. Phys.* **2006**, *125*, 107101.
[85] W. Kutzelnigg, W. Liu, *J. Chem. Phys.* **2005**, *123*, 241102.
[86] K. Andersson, P. Malmqvist, B. O. Roos, *J. Chem. Phys.* **1992**, *96*, 1218–1226.
[87] L. Ungur, M. Thewissen, J.-P. Costes, W. Wernsdorfer, L. F. Chibotaru, *Inorg. Chem.* **2013**, *52*, 6328–6337.
[88] L. F. Chibotaru, L. Ungur, *J. Chem. Phys.* **2012**, *137*, 064112.
[89] L. F. Chibotaru, L. Ungur, A. Soncini, *Angew. Chem. Int. Ed.* **2008**, *47*, 4126-4129.
[90] L. Ungur, L. F. Chibotaru, *Chem. - A Eur. J.* **2017**, *23*, 3708–3718.
[91] M. E. Lines, *J. Chem. Phys.* **1971**, *55*, 2977-2984.
[92] A. B. Castro, J. Jung, S. Golhen, B. Le Guennic, L. Ouahab, O. Cador, F. Pointillart, *Magnetochemistry*, **2016**, *2*, 26.
[93] X. Yi, K. Bernot, V. Le Corre, G. Calvez, F. Pointillart, O. Cador, B. Le Guennic, J. Jung, O. Maury, V. Placide, Y. Guyot, T. Roisnel, C. Daiguebonne, O. Guillou, *Chem. Eur. J.* **2014**, *20*, 1569-1576.
[94] V. Vieru, L. Ungur, L. F. Chibotaru, *J. Phys. Chem. Lett.* **2013**, *4*, 3565–3569.
[95] L. F. Chibotaru, in *Mol. Nanomagnets Relat. Phenom.* **2014**, pp. 185–229.

10.1002/chem.202003556

WILEY-VCH

FULL PAPER

Entry for the Table of Contents

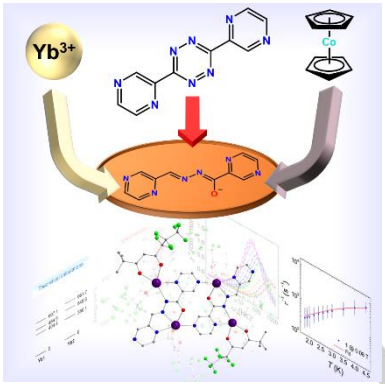

Chemistry is like a box of chocolates: The combination of ytterbium(III), cobaltocene, and 3,6-dipyrazin-2-yl-1,2,4,5-tetrazine (bpztz) lead to an unexpected asymmetric ring opening of the central tetrazine, yielding the first lanthanide-based compound with such an asymmetric opening. The comparison of magnetic and luminescence data with theoretical calculations allowed for accurate and in-depth comparison of the energy levels of the compound.

Institute and/or researcher Twitter usernames: @m_murugesu